processes

MDPI

Article

Influence of Side Duct Position and Venting Position on the Explosion and Combustion Characteristics of Premixed Methane/Air

Junping Cheng [1], Yongmei Hao [1,*], Zhixiang Xing [1], Rui Song [1], Fan Wu [1] and Sunqi Zhuang [2]

[1] College of Safety Science and Engineering, Changzhou University, Changzhou 213164, China; chengjpww11@163.com (J.C.); xingzhixiang@cczu.edu.com.cn (Z.X.); sr00980098@163.com (R.S.); youliahz@163.com (F.W.)
[2] Changzhou Towngas China Company Limited, Changzhou 213000, China; zhuangsqi001@163.com
* Correspondence: hymzcs@cczu.edu.cn

Abstract: In order to explore the influence of the side duct position and venting position on the premixed combustion and explosion characteristics of methane/air, a premixed combustion and explosion experiment of methane/air and a simulation of an explosion of the same size were carried out in a tube with an internal size of 2000 mm × 110 mm × 110 mm. The results showed that the side duct could change the flame structure and accelerate the flame inside the tube. The maximum increase ratio of the flame propagation speed was 106.1%. The side duct had a certain venting effect on the explosion pressure. For different position cases, when the venting film was placed over the bottom section, the maximum overpressure first decreased and then increased. When the venting film was placed over the middle section and the top section, the maximum overpressure first increased and then decreased, and the change trend of the top section was stronger. Turbulence mostly occurred inside the side duct when the venting film of the side duct ruptured. There is no linear relationship between the maximum flame propagation velocity within the tube and the maximum turbulent kinetic energy inside the side duct. The two had a relationship that could be fitted to the Gauss function; the correlation coefficient R^2 was 0.836, and the minimum value was at (4767.72, 17.918), suggesting that the side duct had the best venting effect on the flame inside the duct at this maximum turbulent kinetic energy. The analysis results of the influence of the location of the vent on the maximum flame propagation velocity inside the tube are helpful for optimizing the layout design of the underground space, reducing the combustion efficiency, and ensuring the safety of the process.

Keywords: side duct position; venting; methane/air; explosion characteristics

Citation: Cheng, J.; Hao, Y.; Xing, Z.; Song, R.; Wu, F.; Zhuang, S. Influence of Side Duct Position and Venting Position on the Explosion and Combustion Characteristics of Premixed Methane/Air. *Processes* **2024**, *12*, 538. https://doi.org/10.3390/pr12030538

Academic Editor: Albert Ratner

Received: 6 February 2024
Revised: 22 February 2024
Accepted: 29 February 2024
Published: 8 March 2024

1. Introduction

A leakage of combustible gas, if it mixes with enough air to form a large-scale cloud cluster within the explosion limit and if it is ignited in a local confined space, which would cause a vapor cloud explosion accident, could result in serious casualties and property losses [1]. In particular, vapor cloud explosion accidents in narrow confined spaces such as tunnels, underground pipelines, and utility tunnels are more serious [2–4]. Therefore, using a ventilation tube connected to the side wall for discharge could be a possibility to ensure the safety of industrial processes and reduce the combustion efficiency and the danger of explosions in subterranean spaces [5–7].

For the study of venting duct technology, Barknech, reporting on explosions, stated that the duct could release combustion and explosion energy into a designated area [8]. However, he also discovered that at duct lengths of 10–20 m, flame propagation speeds would exceed the speed of sound and may even cause the transition from deflagration to detonation. Yan et al. used different lengths of long ducts in a closed cylindrical container for venting experiments. It was discovered that the second pressure peak and an external

explosion were caused by the flame igniting the unburned fuel that was washed out of the tube by the pressure wave. The longer the length of the venting duct, the greater the fuel concentration and the greater the secondary explosion intensity [9,10]. Ponizy et al. conducted a series of studies on the flame dynamics in the exhaust vessel connected to the duct and found that the length of the duct affects the turbulent mixing and increases as the length of the duct decreases. At a lower duct length, there was a significant quenching phenomenon in the tube [11–13]. However, a short venting duct that was immediately open to the atmosphere may result in a greater pressure drop [14]. The above research showed that the tube had a certain effect on the discharge process of the explosion in the container. At the same time, in the process, different duct positions brought different discharge effects to the connecting tube and container.

Experts and scholars had conducted a great deal of research on the side venting characteristics of premixed methane–air combustion and explosion [15–18], but in actuality, the position of the side venting port from the ignition source remained uncertain. Yan et al. conducted experiments in a closed cylindrical container with a large aspect ratio and discovered that the side vent closest to the ignition source performed better than the side vent farthest from it [19,20]. Yu et al. and Wan et al. discovered that the side vent had a greater venting effect on the flame propagation through the rectangular tube venting experiment when the flame was in the early stages of accelerated propagation. The better the venting effect was in a particular venting location, the closer the vent was to the ignition source [21–23]. Similarly, Zhou et al. used the large eddy simulation model for a numerical simulation and found that the side vent with a large size near the ignition end had a large venting effect, and the deceleration effect of the side vent on the flame propagation was positively correlated with the venting effect of the side vent [24]. Ajrash et al. used side ducts to conducted an experimental study on the flame deflagration phenomenon of large-scale tubes. They discovered that the side duct had a good venting effect and that the location of the venting was significantly correlated with the flame- and explosion-driving parameters [25].

The above research showed that the position of the side venting was one of the key elements influencing the venting effect, yet research on the venting position of the side duct mainly placed the position of the constraint surface at the end of the venting port, but the position of the constraint surface in the side venting duct might appear at the junction of the duct and the tube or might be inside the side duct. Therefore, this paper took the side duct as the research object and used a self-built experimental platform combined with a FLACS 9.0 software simulation to study the influence of different side duct positions and venting positions on the flame propagation structure, flame propagation velocity, pressure, and turbulent kinetic energy of methane combustion and explosion, so as to provide the relevant technical basis for the specific application of the side duct.

2. Experimental Setup

Figure 1 shows an experimental platform for a methane–air mixed gas explosion, which is mainly composed of five major systems: a data acquisition system, an ignition system, a gas distribution system, a tube system, and various auxiliary facilities. Figure 2 shows the experimental tube. The experimental tube was placed horizontally. The experimental tube had dimensions of 2000 × 110 × 110 mm internally, with a wall thickness of 20 mm. In order to facilitate direct observation, the experimental tube material was made of organic transparent glass. The experimental tube was semi-closed, and the closed end was the ignition end. Before the start of the experiment, 0.1 mm polyethylene film was used as the venting film to seal the open end of the tube and the venting port of the side duct, which were named venting port A and venting port B, respectively, and the air tightness inside the tube was ensured. The A1icat21 series mass flow controller was used to control the gas outflow rate and to fill the gas. The range of the mass flow controller was 0.5sCCM-6000sCCM, and the error range was within ±0.5%. In order to stabilize the methane volume fraction at 9.5%, the gas flow rate of methane was set to be 0.4 L/min,

and the air flow rate was set to be 3.6 L/min. The pressure data acquisition system was mainly composed of a pressure sensor, a signal amplifier, and a data acquisition box. The positive pressure measurement range of the PCB113B21 series piezoelectric pressure sensor was 0–1.38 Mpa, and the accuracy was 0.007 KPa. The pressure sensor was installed at a distance of 600 mm from the closed end. A PHANTOM V1212-72G-C high-speed camera with PCC 3.8 image processing software made up the image data acquisition equipment, which was used to capture the evolution of the flame structure during the methane/air explosion. The shooting frequency was set to 1000 fps. The ignition system was mainly composed of a high-frequency pulse igniter, a pulse switch, and an ignition head. The ignition device adopted a CNQ-10 high frequency pulse igniter, the ignition frequency was 6–12 times/s, and the ignition energy was 10 J. After the mixed gas entered the tube, it was ignited after standing for 60 s, and the ignition time was 1 s.

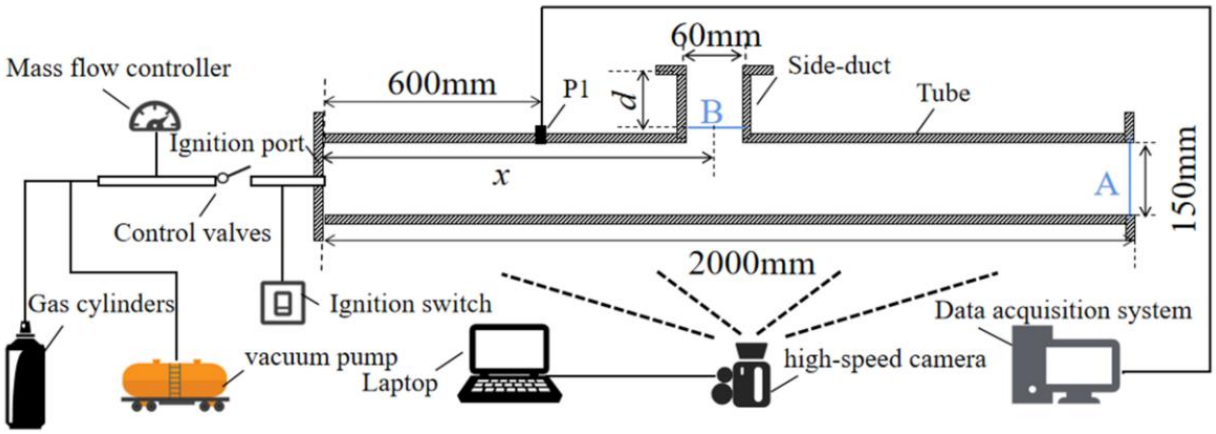

Figure 1. Experiment system structure diagram.

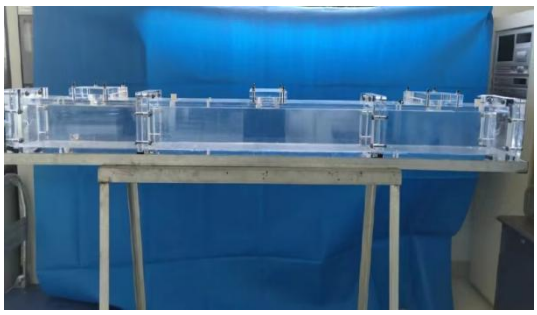

Figure 2. Experiment tube.

It was essential to consider the positions of the side duct and venting film to assess their impact on the characteristics of premixed methane/air combustion and explosion. Front, middle, and end side ducts were placed at the side of the tube at x = 300 mm, x= 1000 mm, and x = 1700 mm from the closed end. The side duct consisted primarily of two ducts, each measuring 50 mm in length, and a bottom plate, resulting in a total length of 120 mm and an inner diameter of 60 mm. This design aimed to facilitate the installation of the venting film. According to the distance d between the venting film and the end of the side duct, the venting films of the bottom, middle, and top sections were named respectively, where d was 100 mm, 50 mm, and 0 mm, respectively. The equivalent experimental case is presented in Table 1, where #1 represents the fundamental control experiment, which involved a premixed gas explosion experiment conducted in without a side duct. Every experimental group had been repeated three times to eliminate the possibility of unexpected outcomes.

Table 1. Experimental settings.

Cases		Without Duct	Side Duct Position (Distance from the Closed End *x*)		
			Front (300 mm)	Middle (1000 mm)	End (1700 mm)
End venting only		#1	-	-	-
Venting position of side duct (Distance from the end of side duct *d*)	Bottom (100 mm)	-	#2	#5	#8
	Middle (50 mm)	-	#3	#6	#9
	Top (0 mm)	-	#4	#7	#10

3. Experimental Results and Analysis

The following experimental data were acquired from the side duct explosion venting experiment with the methane–air mixture at a concentration of 9.5%.

3.1. Flame Structure Evolution

Figure 3 is the flame structure evolution diagram of each case. The flame structure evolution under various cases varied, as could be seen in the image of the flame structure evolution. In Figure 3b, the flame underwent alterations due to its interaction with the side duct, leading to the venting of a portion of the flame through the side duct. This resulted in a diminished luminosity of the #2 flame. The upper flame propagated faster than the lower flame, and the flame shape gradually changed to form an upper inclined flame. The analysis revealed that following the rupture of the film, there was a pressure differential between the interior and exterior of the duct. This variance caused air from the side duct enter the inside of the tube, where it combined with the unburned gas. This interaction led to complete combustion, accelerated the gas flow, and directed the gas from the lower part of the tube towards to the side duct. Therefore, the gas flow rate in the upper part of the tube increased, resulting in the formation of an upper inclined flame. Simultaneously, it could be observed from Figure 3c–j that the upper inclined flame phenomenon happened after the flame flowed through the venting duct. However, the phenomenon was less noticeable the further the side duct was from the ignition point.

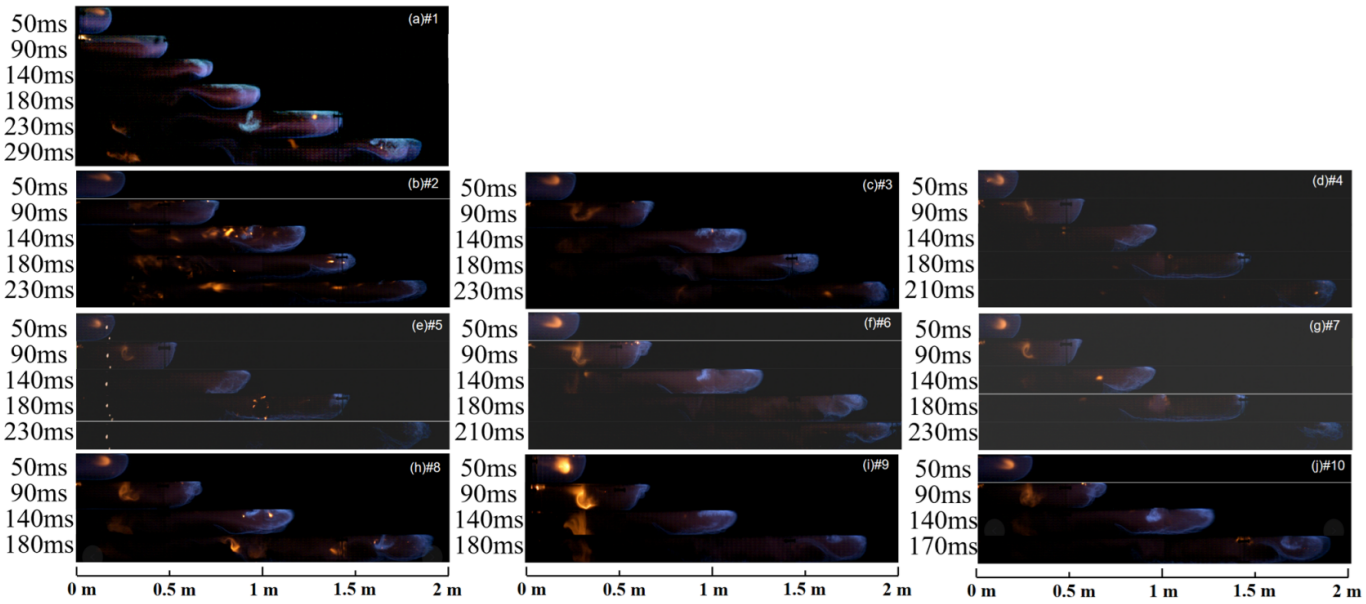

Figure 3. Flame structure evolution diagram of each case.

3.2. Flame Propagation Speed

According to Figure 3, the flame front propagation velocity under different cases was calculated in Matlab, and Figure 4 was obtained. Figure 4a–c show the variation data of the flame front propagation velocity with time under different side duct positions. As can be observed from Figures 3 and 4, the development trend of flame propagation velocity in each case during the early stages of flame propagation is basically identical. After ignition, the flame developed in a hemispherical shape, which increased the flame propagation speed. Following that, the flame made contact with the tube wall, causing its speed of propagation to slow down. The first peak was formed at about 15 ms, and the first velocity peak was 4.38 m/s in the case of no side duct. Turbulence developed after the flame made contact with the tube wall, increasing the rate of local combustion and accelerating propagation of the flame front again. After that, the turbulent flame was transformed into a finger flame, and the flame propagation speed decreased. The second peak was formed at about 70 ms, and the second peak was 8.75 m/s in the case of no side duct. Subsequently, due to the rupture of the venting film, the flame propagation speed grew again under the induction of external air. Compared with the case of no side duct, the flame front propagation velocity was found to be higher at different cases with side duct. This indicated that the side duct could significantly increase the flame propagation velocity.

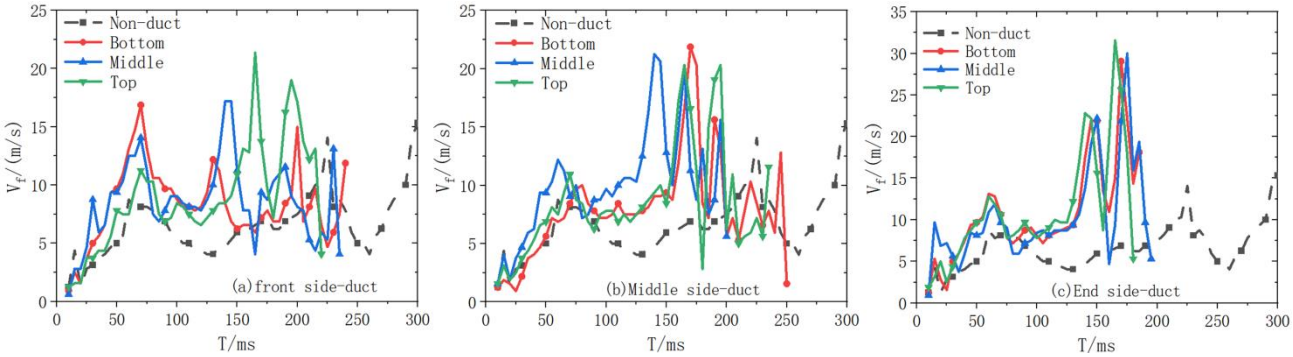

Figure 4. Flame front propagation velocity–time variation under different cases.

The data presented in Figure 4 indicate that the side duct at the end of the tube have the largest maximum flame front propagation velocity among the various side duct positions. This was followed by the side duct at the middle of the tube and, lastly, the side duct at the front of the tube. The maximum flame propagation velocities of the side duct at the end of the tube were 29.06 m/s, 30.00 m/s, and 31.56 m/s, respectively. These values were 89.8%, 95.7%, and 106.1% higher than the case without side duct. Due to the side duct at the end of the tube being far from the ignition point, the flame inside the tube had a longer distance to accelerate when they reached the side duct.

For different venting film positions, when the venting film was located at the top section of the side duct, the maximum flame propagation speeds of the front side duct and the end side duct were the largest, which were 24.38 m/s and 31.56 m/s, respectively. Compared with the case without side duct, the increase ratios were 59.2% and 106.1%, respectively. The occurrence could be attributed to the formation within the side duct during the development of the flame. Specifically, when the venting film was located at the top section of the side duct, the turbulence generated was the largest, resulting in the maximum flame propagation speed.

The flame front of the non-side duct was observed to have an acceleration trend after 130 ms, as seen in Figure 4. The acceleration trend observed was coupled with the flame acceleration effect of the side duct. This led to an increase in the flame front propagation speed of the side duct after 130 ms and formed the maximum flame front propagation speed.

However, when the side duct was located in the middle of the tube, the relationship between the maximum flame propagation velocity exhibited a complete reversal compared

to when the side duct was located in the front and end. It was 21.88 m/s, 20.63 m/s and 20.31 m/s, respectively. Combined with the flame structure evolution image in Figure 3, it was discovered that the flame passes through the side duct in the middle of the tube at a time of approximately 140 ms. Some of the flames were diverted into the side duct due to the presence of unburned gas inside the side duct. The side duct had the maximum space and unburned gas when the venting film was positioned at the top, which led to the greatest amount of diverted flames. But, after 130 ms, it was in the development stage of the maximum flame propagation speed. Due to the diversion of some flames, the maximum flame propagation speed of the side duct in the middle of the tube was reduced. When the venting film was located at the top section of the side duct, the flames were diverted most, resulting in the lowest maximum flame propagation speed.

3.3. Explosion Overpressure inside the Tube

Figure 5 is the pressure changes of the side duct monitoring points P1with time under different cases. Observing the pressure curve without a side duct, the explosion pressure fluctuated obviously. These fluctuations can be attributed to the rupture of the PVC film and occurrence of secondary deflagration at the end of the tube. The pressure curve displayed multiple peak characteristics, and the maximum overpressure at the P1 was 4.680 kPa. Comparing the pressure curve changes of no duct and duct cases, it was obvious that the duct case had more pressure peaks than the no duct case. This difference was due to the PVC film failure and secondary deflagration of the side duct. At the same time, the data showed that the peak value of methane explosion overpressure with side duct was lower than that without side duct, indicating that the side duct could release the explosion overpressure.

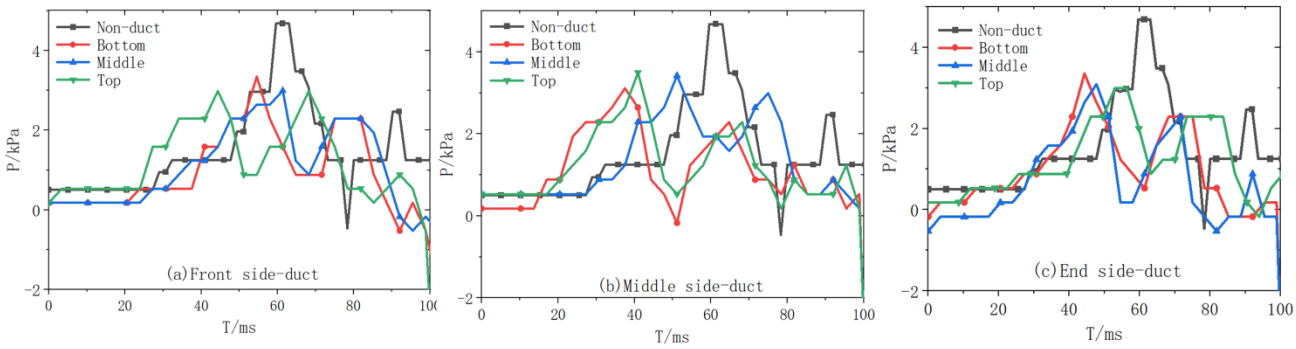

Figure 5. The pressure–time changes of P1 different cases.

Table 2 is the maximum overpressure of side duct under different cases. When the pressure relief effect of side ducts at various positions was compared, the results showed that the effects varied. The venting film at the bottom section provided the best pressure relief effect when the side duct was positioned in the middle of the tube. The explosion pressure of monitoring point P1 dropped by 1.565 kPa, with a decrease ratio of 33.4%. When the side duct was located at the front and end of the tube, optimal pressure relief was achieved by positioning the venting film at the top section. The explosion pressure of the monitoring points P1 dropped by 1.697 kPa and 1.689 kPa, with a decrease ratio of 36.3% and 36.1%.

Comparing the maximum overpressure of different explosion venting positions, Figure 6 shows the maximum overpressure diagram of each monitoring point under different venting film positions. It was found that the maximum overpressure change trend was the same under different monitoring points and different venting film positions.

Table 2. The maximum overpressure inside the tube and the decrease ratio compared with the non-duct case.

Case	*x*/mm	*d*/mm	P_{max}/kPa	Decrease Ratio/%
#1	-	-	4.680	-
#2	300	0	3.345	28.5
#3		50	2.993	36.0
#4		100	2.983	36.3
#5	1000	0	3.115	33.4
#6		50	3.424	26.8
#7		100	3.496	25.3
#8	1700	0	3.351	28.4
#9		50	3.087	34.0
#10		100	2.991	36.1

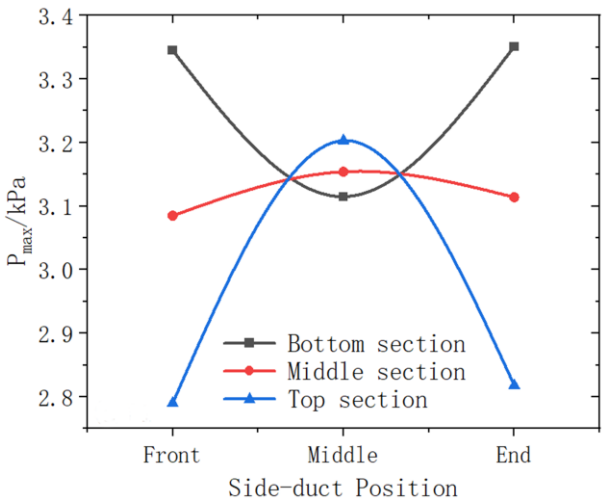

Figure 6. Maximum overpressure at different venting film positions.

When the venting film was located at the bottom section, the maximum overpressure first decreased and then increased. When the side duct was located in the front of the tube, the presence of a specific wall thickness between the bottom of the duct and the inside of the tube caused part of the shock wave to enter the side duct as it passed through the front side duct. At this stage, the shock wave was so weak that it was unable to pass through the venting film. Consequently, a reflected wave was generated, merging with the forward propulsion wave in the tube and propagating to the end of the tube. When the side duct was positioned in the middle of the tube, the strength of the shock wave increased as it passed though the side duct. The venting film at the bottom section was broken, the pressure was released from the side duct, and the pressure release effect was increased. Both the strength and the velocity of the shock wave rose continually when the side duct was at the end of the tube. After the shock wave broke the venting film at the bottom section, the end of the tube venting film was likewise a failure soon after. Most of the shock waves were released from the end of the tube under the induction of inertia and the end venting port, so that the venting effect of the end side duct was poor.

When the venting film was located in the middle section and the top section, the maximum overpressure first increased and then decreased, and the change trend of the top section was stronger. A part of the shock wave entered the side duct when side duct was in the front position and passed through it. The presence of unburned gas inside the side duct led to the induction of the flame into the side duct by the shock wave. This process further strengthened the shock wave, causing a rupture of the venting film and resulting in the formation of a venting effect. With the increase in the distance between the side duct and the ignition source, the maximum overpressure increased continuously, and it was close

to the non-duct case. With the increase in the flame propagation speed, the pressure relief effect reduced because the time for shock wave passing through the side duct shortened. Due to turbulence and the near distance between the side duct and the end of tube, the two venting ports generated a combined effect, increasing the venting effect. There was more unburned gas and space inside the side duct before the failure when the venting film was positioned in the top section than when it was positioned in the middle section. The shock wave was more easily accumulated and developed at the top section, and the venting effect was increased after the rupture of the venting film of the side duct.

4. Numerical Simulation Analysis

In order to further observe the changes in pressure and turbulent kinetic energy in the side duct during tube explosion, the characteristics of methane combustion and explosion in the side duct under different cases were further studied by numerical simulation.

4.1. Geometric Model

Due to the extremely complex explosion process, this work provided several appropriate simplified assumptions in order to conduct a numerical simulation using FLACS software: The gas in the confined space satisfied the real gas state equation. The specific heat capacity of the combustion gas mixture changed with temperature, which satisfied the mixing rule. The explosion process of combustible gas was a single-step reaction. The explosion process was an adiabatic process, without considering the heat exchange between the confined space and the outside environment.

The state parameters in the process of combustible gas explosion followed the three equations of mass, momentum and energy conservation, and continuity equation and other control equations. The governing equation could be expressed as Equation (1):

$$\frac{\partial}{\partial t}(\rho\varphi) + \frac{\partial}{\partial x_i}(\rho u_i \varphi) = \frac{\partial}{\partial x_i}(\Gamma_\varphi \frac{\partial \varphi}{\partial x_i}) + S_\varphi \quad (1)$$

Among them, t is the time, s; ρ is the density, kg/m^3; x_i is the space coordinates, m; u_i is the velocity at the direction of x_i, m/s; φ is the general variable; S_φ is the source term; and Γ_φ is the diffusion coefficient.

Turbulence was calculated by a two-equation model, the k-ε model. It was an eddy viscosity model that solved two additional transport equations, which were kinetic energy and dissipation of turbulent kinetic energy, defined as Equations (2) and (3) [26]:

$$\frac{\partial}{\partial t}(\rho k) + \frac{\partial}{\partial x_i}(\rho u_i k) = \frac{\partial}{\partial x_j}(\frac{\mu_{eff}}{\sigma_k}\frac{\partial k}{\partial x_i}) + G - \rho\varepsilon \quad (2)$$

$$\frac{\partial}{\partial t}(\rho \varepsilon) + \frac{\partial}{\partial x_i}(\rho u_i \varepsilon) = \frac{\partial}{\partial x_i}(\frac{\mu_{eff}}{\sigma_\varepsilon}\frac{\partial \varepsilon}{\partial x_i}) + C_1 G - C_2 \rho \frac{\varepsilon^2}{k} \quad (3)$$

Among them, k is the turbulent kinetic energy, m^2/s^2; ε is the turbulent kinetic energy dissipation rate, m^2/s^3; μ_{ef} is the effective viscosity, Pa·s; C_1, C_2, σ_k, and σ_ε are the model constants, the value of which are 1.44, 1.92, 1.3, and 1.0, respectively; and G is the generating term of turbulent kinetic energy.

4.1.1. Geometric Model and Parameter Setting

The geometric model was built according to the size of the experimental tube. A semi-closed square tube with an internal size of 2000 mm × 110 mm × 110 mm was established along the X-axis with the ignition point O (0,0,0) as the end point, and the wall thickness of the tube was 20 mm. The simulation case configuration was consistent with the experimental case.

(1) Monitoring point setting. In order to more accurately observe the relationship between turbulent kinetic energy and time at a certain point in space, monitoring point P2 was

set in the tube. To facilitate a more intuitive observation of the variations in turbulent kinetic energy inside the side duct, monitoring point P2 was set at 25 mm from the end of the side duct.

(2) Output variable setting. In order to facilitate the analysis of the change in methane explosion characteristics in the side duct with time, it was necessary to set the relevant 2D and 3D output variables and to select the turbulent kinetic energy as the output variables.

(3) Boundary condition setting. The boundary conditions were Euler equations. The initial temperature in the tube was 20 °C, the atmospheric pressure was 10^5 Pa, and the gravitational acceleration was 9.8 m/s^2. In order to be close to experimental cases, the type of venting film was "POPOUT", and the venting pressure was set to 2 kPa.

(4) Explosive gas setting. To accurately replicate the conditions, a methane/air mixture with an equivalence ratio of 1, where methane comprised 9.5% of the mixture, was utilized. This explosive gas was then introduced into the tube.

(5) Ignition area setting. The ignition point was located in the center of the closed end.

4.1.2. Grid Independence and Model Accuracy Verification

The vapor cloud explosion simulation of FLACS has high precision and low error, which could be used to simulate the explosion in a complex space [27]. The simulation results for the methane–air mixture explosion are extremely similar to the experimental values, especially in confined space [28].

The experimental data and numerical simulation results without a side duct were compared and analyzed. To confirm the grid independence and the accuracy of the model, 4 mm, 5 mm, 6 mm, and 7.5 mm grids were selected to compare with the experimental results. Figure 7 shows the pressure–time curve under different grid sizes. It could be seen that the four different grid sizes could better simulate the characteristics of methane/air explosion pressure changing with time.

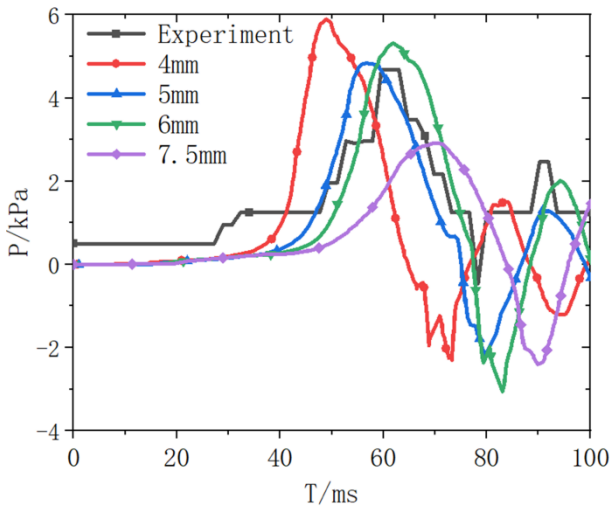

Figure 7. Pressure–time changes under different mesh sizes.

Table 3 shows the overpressure peak at the monitoring point P1 under different grid sizes. Table 3 indicates the overpressure peak of the 5 mm grid size, which is 4.838 kPa with a 3.4% calculation error. Compared to other grids, the calculation accuracy is higher, indicating that the 5 mm grid is sufficient. Figure 8 is the geometric model and meshing map under 5 mm mesh.

Table 3. Overpressure peaks under different grid cases.

Cases	Overpressure Peak/kPa	Relative Error/%
Experiment	4.680	-
4 mm grid	5.895	26.0
5 mm grid	4.838	3.4
6 mm grid	5.321	13.7
7.5 mm grid	2.916	37.7

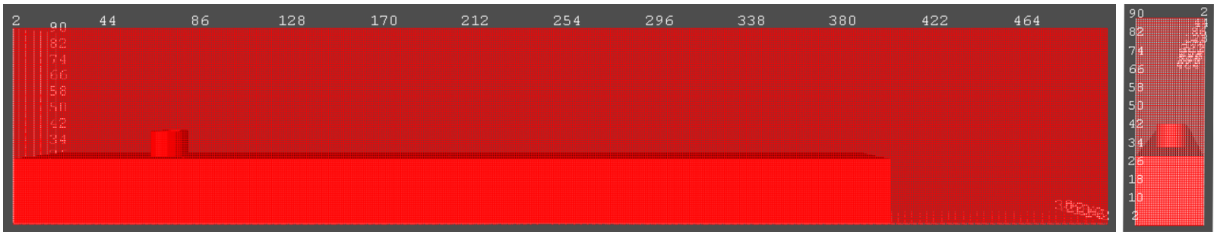

Figure 8. The 5 mm mesh geometry model and mesh generation diagram.

Combined with the analysis of Figure 7 and Table 3, the peak pressure of numerical simulation using a 5 mm grid was basically consistent with the experimental results. However, there was a discrepancy in the timing of the overpressure peak, which occurred earlier in the simulation. The main reason for the error stemmed from the adiabatic process of the explosion process, which neglected the heat exchange with the external environment. Consequently, the peak overpressure time in the numerical simulation occurred earlier than in the experiment date. But, on the whole, the predicted explosion pressure in the numerical simulation was basically consistent with the experimental results. As a result, the numerical model had great accuracy, and FLACS could be used to simulate the explosion process of premixed gas in confined space.

4.2. Numerical Simulation Results and Analysis

Turbulent Kinetic Energy inside the Side Duct

When the explosion gas propagated in the tube, the propagation direction and velocity gradient of the explosion gas flow changed due to various factors such as explosion shock waves, flames, and obstacles, forming turbulence. The change in turbulent kinetic energy with time reflected the net income and expenditure of turbulent kinetic energy, which was an index to measure the development or decline of turbulence. The distribution of turbulent kinetic energy within the side duct under various numerical simulation cases is depicted in Figure 9. At the beginning of the explosion, turbulence appeared at the front end of the flame front, but after the rupture of the side duct venting film, turbulence mainly appeared inside the side duct. From Figure 9, it can be seen that the turbulent kinetic energy would form a turbulent vortex on the right side of the side duct under different cases. Therefore, the disturbance source can be considered to be the right inflection point of the side duct. This disturbance source led the gas flow rate to increase inside the side duct, inducing a large amount of tube gas into the side duct. A venting effect happened at the same time the shock wave and flame in the tube entered the side duct.

Figure 10 shows the comparison data of the turbulent kinetic energy of monitoring point P2 in different cases of side duct. In Figure 10, the side duct in front of the tube has the highest turbulent kinetic energy under various position cases, and the side duct that is closest to the ignition point has a higher turbulent kinetic energy. This showed that the closer the ignition source of the side duct, the more unburned gas was released to the outside. The unburned gas burned inside the side duct. The combustion process and the gas flow interacted in a positive feedback coupling effect, leading to a continuous increase in the flow field gradient, resulting in an increase in turbulent kinetic energy. In various cases of venting film position, the turbulent kinetic energy in the front and end side ducts

of the tube was found to be highest when the venting film was placed over the top section. Conversely, the side duct placed in the middle of the tube exhibited the highest turbulent kinetic energy when the venting film was placed over the bottom section. This observation contrasts with the maximum flame propagation velocity inside the tube. It showed that the maximum flame propagation velocity inside the tube would be affected by maximum turbulent kinetic energy to a certain extent.

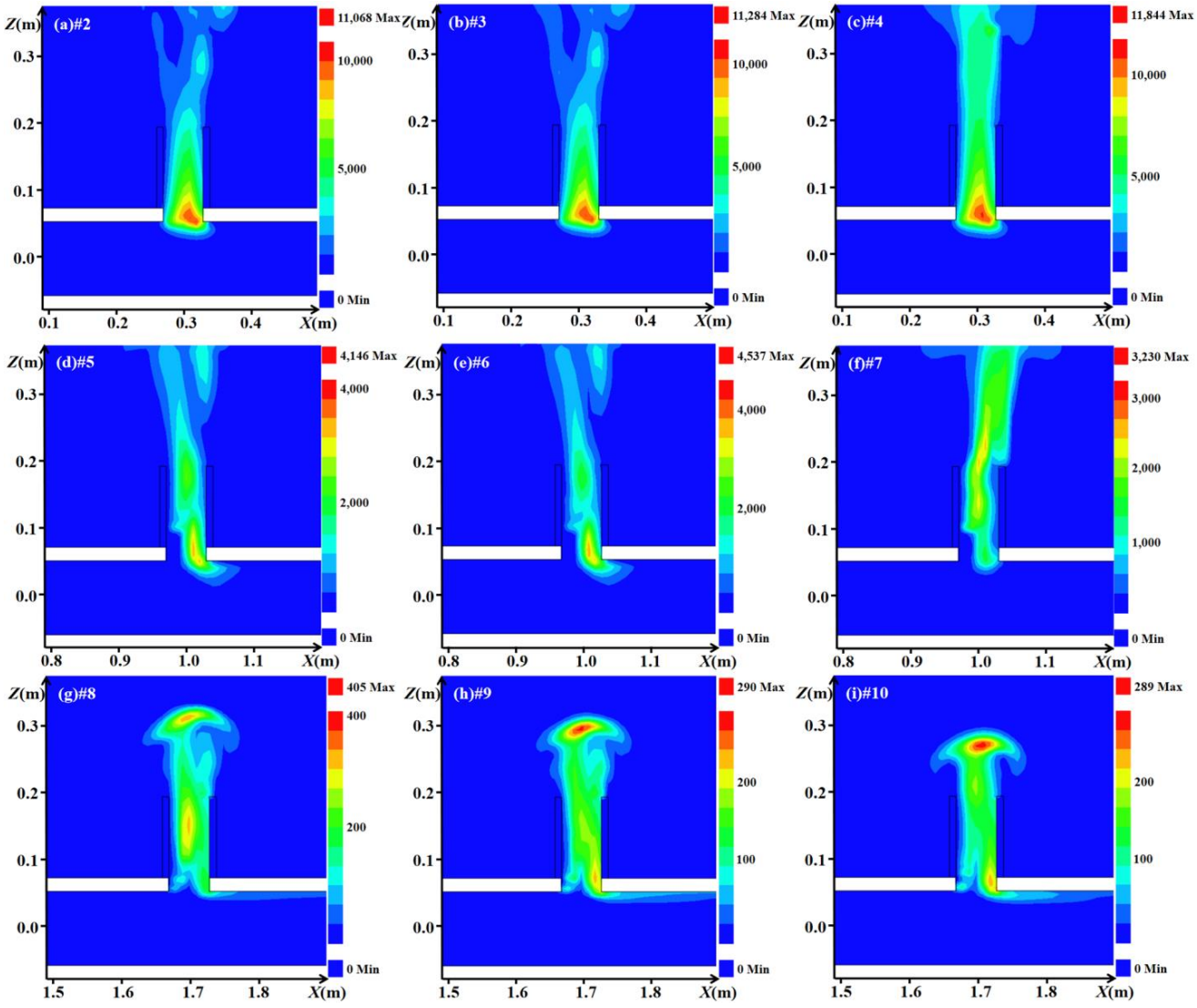

Figure 9. Turbulent kinetic energy distribution inside the duct under different case.

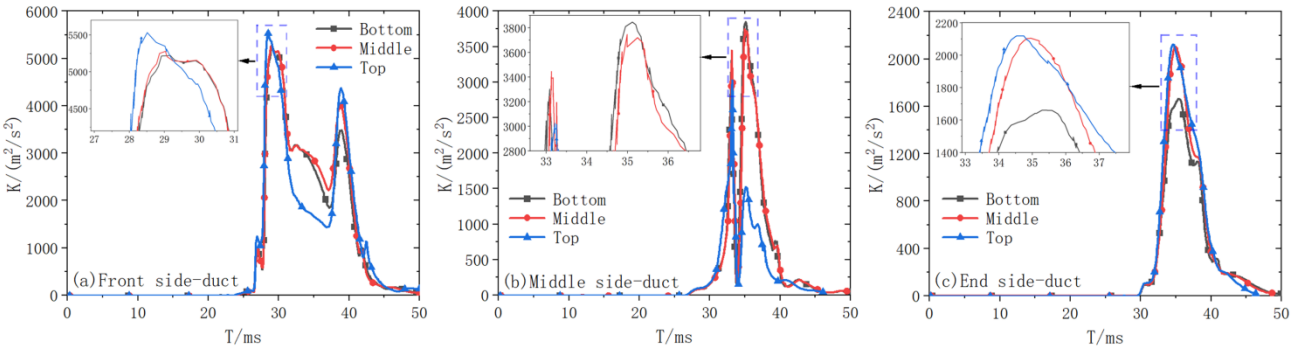

Figure 10. Turbulent kinetic energy–time change at the end of the duct under different cases.

4.3. Coupling Relationship between Maximum Flame Propagation Velocity and Maximum Turbulent Kinetic Energy

The side duct could obviously accelerate the flame inside the tube, and the turbulence inside the side duct was one of the important factors affecting the flame propagation speed. Figure 11 is the fitting curve of the maximum flame propagation velocity inside the tube and the maximum turbulent kinetic energy inside the side duct.

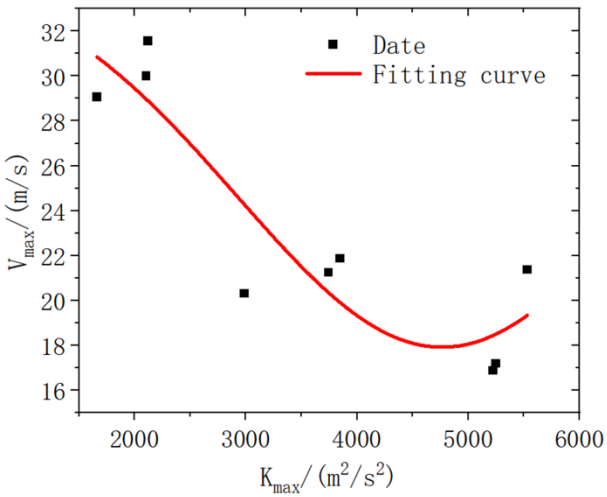

Figure 11. Fitting curves of maximum flame propagation velocity and maximum turbulent kinetic energy.

As shown in Figure 11, the relationship between the maximum flame propagation velocity inside the tube and the maximum turbulent kinetic energy inside the side duct could be fitted as a Gauss function, as shown in Equation (4):

$$V_{max} = 34.940 - \frac{78412.992}{3675.594 \times \sqrt{\pi/2}} \times \exp\left(-\frac{(K_{max} - 4764.043)^2}{6475995.626}\right) \quad (4)$$

Among them, V_{max} is the maximum flame propagation velocity inside the tube, m/s and K_{max} is the maximum turbulent kinetic energy inside the side duct, m^2/s^2. The correlation coefficient R^2 of the fitting equation was 0.836, and the fitting was successful and the fitting effect was good.

The curve fitting analysis indicated that as the turbulent kinetic energy increased inside the side duct, the maximum flame propagation velocity inside the duct first decreased and then increased. When the maximum turbulent kinetic energy inside the side duct was 4767.72 m^2/s^2, the maximum flame propagation speed inside the tube was the smallest, which was 17.918 m/s. At this time, the side duct had the best effect on the release of flame inside the tube.

The turbulent kinetic energy inside the side duct was affected by the side duct position and the venting film position. According to the relevant experimental data in Figure 11, the minimum value of the maximum flame propagation speed is 16.875 m/s. The side duct was located 300 mm from the ignition point, and the venting film was located at the bottom of the side duct. The maximum turbulent kinetic energy was 5221.510 m^2/s^2. Consequently, the inflection point on the fitting curve, representing the minimum value on the fitting curve, indicated that the side duct was located near 300 mm from the ignition point, falling within the range of over 300 mm but less than 1000 mm.

5. Conclusions

In this paper, methane–air mixed gas explosion experiments at different positions and venting positions of the side duct were carried out to observe the flame structure, flame propagation speed, and pressure changes inside the duct. On the basis of the experiment, FLACS was used to simulate the turbulent kinetic energy inside the side duct under different cases. Based on the experimental and numerical analysis results, the following conclusions were drawn:

(1) Compared with the case without a side duct, the side duct could obviously accelerate the flame inside the tube. Turbulence and flame velocity trends both had an effect on the maximum flame propagation velocity within the tube. When the side duct was located in the middle of the tube, the flame diversion phenomenon caused by turbulence coincides with the acceleration trend inside the tube, which reduced the growth rate of the maximum flame propagation speed under this case.

(2) When the venting film was located at the top section of the side duct, the pressure relief effect of the front side duct was the best. For different position cases, when the venting film was located at the bottom section, the maximum overpressure first decreased and then increased. When the venting film was located in the middle section and the top section, the maximum overpressure first increased and then decreased, and the change trend of the top section was stronger.

(3) Turbulence mostly occurred inside the side duct when the venting film failure of the side duct and the side duct formed a venting effect under the action of turbulence. There is no linear relationship between the maximum flame propagation velocity within the tube and the maximum turbulent kinetic energy inside the side duct. The relationship between the two could be fitted as a Gauss function; the minimum value was at (4767.72, 17.918), indicating that the side duct was located near 300 mm from the ignition point; and the side duct had the best effect on the release of flame inside the tube.

Author Contributions: Conceptualization, J.C. and Y.H.; Methodology, Y.H.; Software, J.C.; Validation, J.C., F.W. and S.Z.; Formal Analysis, J.C.; Investigation, R.S.; Resources, Z.X.; Data Curation, R.S.; Writing—Original Draft Preparation, J.C.; Writing—Review and Editing, Y.H.; Visualization, J.C.; Supervision, Z.X.; Project Administration, F.W.; Funding Acquisition, S.Z. All authors have read and agreed to the published version of the manuscript.

Funding: This research has been supported by the Natural Science Foundation of the Jiangsu Higher Education Institutions of China (23KJB620001), the Changzhou Social Development Science and Technology Support Project (CE20225033), and the Key R&D projects in Jiangsu Province (BE2021641).

Data Availability Statement: The research data are presented in this paper.

Conflicts of Interest: We declare that we have no known competing financial interests or personal relationships that could have appeared to influence the work reported in this paper. Author Sunqi Zhuang was employed by the Changzhou Towngas China Company Limited. The authors declare that the research was conducted in the absence of any commercial or financial relationships that could be construed as a potential conflict of interest.

References

1. Moreno, V.C.; Danzi, E.; Marmo, L.; Salzanoa, E.; Cozzani, V. Major accident hazard in biodiesel production processes. *Safety Sci.* **2019**, *113*, 490–503. [CrossRef]
2. Jackson, R.B.; Down, A.; Phillips, N.G.; Ackley, R.C.; Cook, C.W.; Plata, D.L.; Zhao, K.G. Natural Gas Pipeline Leaks Across Washington, DC. *Environ. Sci. Technol.* **2014**, *48*, 2051–2058. [CrossRef] [PubMed]
3. Dursun, A.E. Statistical analysis of methane explosions in Turkey's underground coal mines and some recommendations for the prevention of these accidents: 2010–2017. *Nat. Hazards* **2020**, *104*, 329–351. [CrossRef]
4. Sanmiquel-Pera, L.; Bascompta, M.; Anticoi, H.F. Analysis of a Historical Accident in a Spanish Coal Mine. *Int. J. Environ. Res. Public Health* **2019**, *16*, 3615. [CrossRef] [PubMed]
5. Xu, Y.; Huang, Y.M.; Ma, G.W. A review on effects of different factors on gas explosions in underground structures. *Undergr. Space* **2020**, *5*, 298–314. [CrossRef]

6. Chao, J.; Bauwens, C.R.; Dorofeev, S.B. An analysis of peak overpressures in vented gaseous explosions. *Proc. Combust. Inst.* **2011**, *33*, 2367–2374. [CrossRef]
7. Lamioni, R.; Bronzoni, C.; Folli, M.; Tognotti, L.; Galletti, C. Impact of H_2-enriched natural gas on pollutant emissions from domestic condensing boilers: Numerical simulations of the combustion chamber. *Int. J. Hydrogen Energy* **2023**, *48*, 19686–19699. [CrossRef]
8. Barknech, W. *Explosions*; Springer: Berlin/Heidelberg, Germany, 1993.
9. Yan, X.Q.; Li, D.; Yu, J.L. Secondary explosions in relief duct during aluminum dust explosion venting. *Procedia Eng.* **2012**, *45*, 431–434. [CrossRef]
10. Yan, X.Q.; Yu, J.L.; Gao, W. Duct-venting of dust explosions in a 20 L sphere at elevated static activation overpressures. *J. Loss Prevent. Proc.* **2014**, *32*, 63–69. [CrossRef]
11. Ponizy, B.; Leyer, J.C. Flame dynamics in a vented vessel connected to a duct: 1. Mechanism of vessel-duct interaction. *Combust. Flame* **1999**, *116*, 259–271. [CrossRef]
12. Ponizy, B.; Leyer, J.C. Flame dynamics in a vented vessel connected to a duct: 2. Influence of ignition site, membrane rupture, and turbulence. *Combust. Flame* **1999**, *116*, 272–281. [CrossRef]
13. Ponizy, B.; Veyssiere, B. Mitigation of explosions in a vented vessel connected to a duct. *Combust. Sci. Technol.* **2000**, *158*, 167–182. [CrossRef]
14. Russo, P.; Di Benedetto, A. Effects of a duct on the venting of explosions—Critical review. *Process Saf. Environ. Prot.* **2007**, *85*, 9–22. [CrossRef]
15. Cao, Y.; Gao, K.H.; Li, B.; Xie, L.F.; Pan, X.H. Influence of vent size and vent burst pressure on vented ethylene-air explosion: Experimental and numerical study. *Process Saf. Environ. Prot.* **2023**, *170*, 297–309. [CrossRef]
16. Lu, Y.W.; Wang, Z.R.; Cao, X.Y.; Cui, Y.Y.; Sun, P.P.; Qian, C.J. Interaction mechanism of wire mesh inhibition and ducted venting on methane explosion. *Fuel* **2021**, *304*, 121343. [CrossRef]
17. Wang, Q.H.; Jin, S.L.; Luo, Z.M.; Dai, A.P.; Wang, Q.F.; Li, Z.H. Flame propagation characteristics of methane explosion under different venting conditions. *Fuel* **2023**, *334*, 126721. [CrossRef]
18. Cao, W.G.; Li, W.J.; Yu, S.; Zhang, Y.; Shu, C.M.; Liu, Y.F.; Luo, J.W.; Bu, L.T.; Tan, Y.X. Explosion venting hazards of temperature effects and pressure characteristics for premixed hydrogen-air mixtures in a spherical container. *Fuel* **2021**, *290*, 120034. [CrossRef]
19. Alexiou, A.; Andrews, G.E.; Phylaktou, H. A comparison between end-vented and side-vented gas explosions in large L/D vessels. *Process Saf. Environ. Prot.* **1997**, *75*, 9–13. [CrossRef]
20. Alexiou, A.; Andrews, G.E.; Phylaktou, H. Side-vented gas explosions in a long vessel: The effect of vent position. *J. Loss Prev. Process Ind.* **1996**, *9*, 351–356. [CrossRef]
21. Yu, M.G.; Wan, S.J.; Zheng, K.; Guo, P.K.; Chu, T.X.; Wang, C.Y. Effect of side venting areas on the methane/air explosion characteristics in a pipeline. *J. Loss Prevent. Proc.* **2018**, *54*, 123–130. [CrossRef]
22. Yu, M.G.; Wan, S.J.; Zheng, K.; Guo, P.K.; Chu, T.X.; Yuan, Z. Influence on the methane/air explosion characteristics of the side venting position in a pipeline. *Process Saf. Environ. Prot.* **2017**, *111*, 292–299. [CrossRef]
23. Wan, S.J.; Yu, M.G.; Zheng, K.; Xu, Y.L.; Yuan, Z.; Wang, C.Y. Influence of obstacle blockage on methane/air explosion characteristics affected by side venting in a duct. *J. Loss Prevent. Proc.* **2018**, *54*, 281–288. [CrossRef]
24. Zhou, N.; Mei, Y.; Li, X.; Chen, B.; Huang, W.Q.; Rasouli, V.; Zhao, H.J.; Yuan, X.J. Numerical Simulation of the Influence of Vent Conditions on Hydrogen Flame Propagation. *Combust. Sci. Technol.* **2021**, *193*, 2331–2349. [CrossRef]
25. Ajrash, M.J.; Zanganeh, J.; Moghtaderi, B. Flame deflagration in side-on vented detonation tubes: A large scale study. *J. Hazard Mater.* **2018**, *345*, 38–47. [CrossRef] [PubMed]
26. GexCon; FLACS-CFD, Explosion & Dispersion Modelling Software. 2021. Available online: https://www.gexcon.com/software/flacs-cfd/ (accessed on 20 February 2024).
27. Xu, Y.; Huang, Y.M.; Li, J.D.; Ma, G.W. A risk-based optimal pressure relief opening design for gas explosions in underground utility tunnels. *Tunn. Undergr. Space Technol.* **2021**, *116*, 104091. [CrossRef]
28. Zhang, Q.T.; Zhou, G.; Hu, Y.Y.; Wang, S.C.; Sun, B.; Yin, W.J.; Guo, F.S. Risk evaluation and analysis of a gas tank explosion based on a vapor cloud explosion model: A case study. *Eng. Fail. Anal.* **2019**, *101*, 22–35. [CrossRef]